Biochemistry

Article

Cite This: Biochemistry 2019, 58, 1226−1235

pubs.acs.org/biochemistry

Interaction between Cellobiose Dehydrogenase and Lytic Polysaccharide Monooxygenase

Christophe V. F. P. Laurent,[†,‡] Erik Breslmayr,[†,‡] Daniel Tunega,[§] Roland Ludwig,[‡] and Chris Oostenbrink*[,†]

[†]Institute of Molecular Modeling and Simulation, BOKU-University of Natural Resources and Life Sciences, 1190 Vienna, Austria

[‡]Vienna Institute of BioTechnology, BOKU-University of Natural Resources and Life Sciences, 1190 Vienna, Austria

[§]Institute of Soil Research, BOKU-University of Natural Resources and Life Sciences, 1190 Vienna, Austria

Supporting Information

ABSTRACT: Lytic polysaccharide monooxygenases (LPMOs) are ubiquitous oxidoreductases, facilitating the degradation of polymeric carbohydrates in biomass. Cellobiose dehydrogenase (CDH) is a biologically relevant electron donor in this process, with the electrons resulting from cellobiose oxidation being shuttled from the CDH dehydrogenase domain to its cytochrome domain and then to the LPMO catalytic site. In this work, we investigate the interaction of four *Neurospora crassa* LPMOs and five CDH cytochrome domains from different species using computational methods. We used HADDOCK to perform protein−protein docking experiments on all 20 combinations and subsequently to select four complexes for extensive molecular dynamics simulations. The potential of mean force is computed for a rotation of the cytochrome domain relative to LPMO. We find that the LPMO loops are largely responsible for the preferred orientations of the cytochrome domains. This leads us to postulate a hybrid version of *Nc*LPMO9F, with exchanged loops and predicted altered cytochrome binding preferences for this variant. Our work provides insight into the possible mechanisms of electron transfer between the two protein systems, in agreement with and complementary to previously published experimental data.

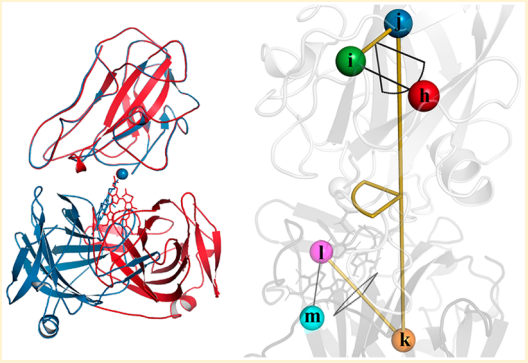

Biomass is an abundantly accessible raw material and therefore triggers continuous efforts to promote renewable energies such as biofuel. A major portion of the available biomass is composed of lignocellulose. Because of the insoluble crystalline nature of the cellulose, the glycosidic linkages are protected from hydrolytic enzymes such as cellobiohydrolases. In addition, the combination of pretreatment and enzymatic processing remains a major hurdle in the production of fermentable sugars.[1] However, the discovery that copper-dependent lytic polysaccharide monooxygenases (LPMO, CAZy auxiliary activity families AA9−AA11 and AA13−AA15) can potentiate the activity of hydrolytic enzymes by increasing the substrate accessibility opens new possibilities.[2−10] The substrate accessibility of hydrolytic enzymes is being improved by the oxidative cleavage of the polysaccharide backbone performed by LPMO.[5] The details of the underlying mechanism are still under investigation, especially the nature of the co-substrate that has been reported to be either molecular oxygen or hydrogen peroxide.[3,5,11−14] Nonetheless, studies have agreed that an electron donor is needed to reduce the active-site copper in LPMO prior to the activation of the oxygen species. Reduction of the LPMO Cu(II) center has been reported to occur over several possible routes, which include small molecular reductants of fungal and plant origin as well as photosynthetic pigments.[5,15−17] Another electron transfer system includes extracellular proteins that reduce the LPMO Cu(II) center either directly [e.g., flavocytochrome cellobiose dehydrogenase (CDH; CAZy family AA3.1)] or indirectly through redox mediators that can be recycled by glucose-methanol-choline (GMC) oxidoreductase family enzymes (CAZy subfamily AA3.2).[5,11,12,17] In the case of CDH, the electron transfer chain is starting at the dehydrogenase domain (DH) containing flavin adenine dinucleotide (FAD) where two electrons are gained by the oxidation of cellobiose into cellobionolactone.[18] In a subsequent interdomain electron transfer, one electron is being passed from the FAD to heme *b* of the cytochrome domain (CYT).[11,19−22] In the open state, the CYT is connected to the DH domain via a flexible linker.[11] This allows the CYT to interact largely independently with the LPMO and reduce the Cu(II).[11,17] It has been proposed that the CYT interaction site is located in the vicinity of a conserved PGP motif on the LPMO surface.[23] In such a model, the electron would follow a path from CYT heme *b* through the LPMO over several amino acids toward the Cu(II) center, allowing the simultaneous binding of the

Received: November 12, 2018
Revised: January 24, 2019
Published: February 4, 2019

DOI: 10.1021/acs.biochem.8b01178
Biochemistry 2019, 58, 1226−1235

substrate and CYT to LPMO. Conversely, in a direct electron transfer model, the electron transfer occurs directly between CYT heme *b* and the LPMO Cu(II) and would not allow concurrent interaction of LPMO with its polysaccharide substrate and CYT. The latter model is supported by experimental data reporting an overlap in the interaction surface patches for the substrate and CYT on LPMO.[24] However, the amino acids involved in the interaction between LPMO and CYT were limited to a narrow surface patch around the LPMO active center that is pointing to a transient and promiscuous interaction.[24] A direct interaction between CYT heme *b* and LPMO copper center was also recently confirmed by small angle X-ray scattering data.[25] Here we use computer models to investigate the most likely interaction of the CYT and LPMO. We have performed protein−protein docking experiments for all combinations of a set of five related CYTs and four LPMO catalytic domains. The optimal relative orientation was further studied using molecular dynamics (MD) simulations and free energy calculations. On the basis of the results, we suggest that the interaction between the CYT and LPMO is guided by the loops that surround the LPMO active site.

METHODS

Protein Structures. For the cytochrome domains, the crystal structures of *Neurospora crassa* CDHIIA [*Nc*CDHIIA; Protein Data Bank (PDB) entry 4qi7], *Crassicarpon hotsonii* (syn. *Myriococcum thermophilum*) CYT (*Ch*CYT; PDB entry 4qi3), and *Phanerochaete chrysosporium* CYT (*Pc*CYT; PDB entry 1d7b) were used. In the case of *Nc*CDHIIA, only the CYT residues (T2−C211) and heme *b* of the model were retained (*Nc*CYTIIA). The amino acid sequences of *N. crassa* CDHIIB CYT (*Nc*CYTIIB; UniProt entry Q7S0Y1) and *Crassicarpon thermophilum* (syn. *Corynascus thermophilus*) CDHIIB CYT (*Ct*CYT; UniProt entry E7D6B9) were modeled onto the crystal structure of *Ch*CYT (PDB entry 4qi6) using SWISS-MODEL.[26−28] For *Nc*CYTIIB, residues Q1−T212 were modeled with a QMEAN4 *z*-score of −4.01, and for *Ct*CYT, we used residues Q1−T203, leading to a QMEAN4 *z*-score of −2.94. Subsequently, the heme *b* cofactor was fitted into the models using the PyMOL Molecular Graphics System (version 1.7.0.0, Schrödinger, LLC). After an initial steepest descent minimization with a convergence criterion of 0.1 kJ mol^{-1} using the GROMOS software package for molecular simulation[29] together with the 54A7 force field,[30] MD simulations were performed as described below for 30 and 100 ns of the resulting *Nc*CYTIIB and *Ct*CYT models, respectively. The coordinates were clustered according to their root-mean-square deviation (RMSD) using 0.12 and 0.15 nm cutoffs to create 10 clusters for *Nc*CYTIIB and *Ct*CYT, respectively. The resulting clusters were used as input coordinates for the molecular docking experiments described below.

For LPMO, the crystal structures of *N. crassa* LPMO9C, -9D, -9F, and -9M were used: *Nc*LPMO9C (PDB entry 4d7u), *Nc*LPMO9D (PDB entry 4eir), *Nc*LPMO9F (PDB entry 4qi8), and *Nc*LPMO9M (PDB entry 4eis). To create the structure of a suggested *Nc*LPMO9F$_{loop}$ variant, the three-dimensional coordinates of *Nc*LPMO9F residues G66−P68 were replaced by those of *Nc*LPMO9C residues F61−N77. As a further refinement, the *Nc*LPMO9F$_{loop}$ structure was relaxed by steepest descent energy minimization with a convergence criterion of 0.1 kJ mol^{-1}.

Molecular Docking. Protonation states of each molecule at pH 6.0 were calculated with PROPKA3,[31−33] and molecular docking was performed with HADDOCK 2.2.[34,35] HADDOCK distinguishes between *ab initio* docking and restraint docking, in which ambiguous interaction restraints can be used to guide the docking process. Furthermore, HADDOCK uses multiple stages of docking, in which an initial rigid body docking is followed by a semiflexible refinement docking stage. To limit the interaction surface of the CYT to the cofactor facing site during *ab initio* docking, only selected residues were made available for random ambiguous interaction restraints (Table S1) while all accessible residues of LPMO were considered for random ambiguous interaction restraints. To force contact between the two molecules, center of mass restraints were switched on, whereas the interaction between heme *b* and the LPMO Cu(II) center had to be satisfied during restraint docking experiments. The numbers of structures for rigid body dockings were set to 10^4 and 10^3 solutions for *ab initio* and restraint docking, respectively. Subsequently, 200 solutions were considered for semiflexible docking during both *ab initio* and restraint docking. The terms of the HADDOCK scoring function were weighted as described in Table S2. Restraint docking was repeated with three different seeds, and docking solutions were clustered according to their RMSD using a 0.15 nm cutoff. The final docking solutions were further analyzed with the GROMOS++ software package.[36]

Molecular Dynamics Simulation Settings. The optimized relative orientation of CYT and LPMO was further studied by computing the potential of mean force (PMF) of rotation around a defined axis.[37] All MD simulations were performed with the GROMOS11 biomolecular simulation package.[29] The starting coordinates were taken from the best ranked restraint docking solution for complexes with *Nc*CYTIIA, *Ch*CYT, *Nc*LPMO9C, *Nc*LPMO9F, and *Nc*LPMO9F$_{loop}$. The PyMOL Molecular Graphics System (version 1.7.0.0, Schrödinger, LLC) was used to create sets of 36 input coordinates for each pair by rotating the individual molecules in 10° steps relative to each other around the axis given by the LPMO center of mass and its Cu(II) atom. The resulting structures were parametrized using the GROMOS++ software package[36] with the GROMOS 54A7 force field.[30] Heme *b* was parametrized in its reduced form using the parameters described by Zou et al.[38] Partial atomic charges around the copper ion of LPMO were obtained from density functional theory (DFT) calculations on the Cu(II) center and its coordination ligands (*Nc*LPMO9F, H1, H72, and Y157). The geometry of the LMPO fragments was derived from the *Nc*LPMO9F crystal structure (PDB entry 4qi8); in the DFT calculation, the Cu(II) coordination was kept fixed and only atoms of ligands were optimized. The calculations were performed by means of the Gaussian package[39] using the PBE functional[40] and the def2-TZVP atomic basis set.[41] The partial atomic charges were obtained from natural population analysis[42] and are listed in Figure S1.

Subsequently, the parametrized complexes were subjected to two *in vacuo* steepest descent energy minimizations with a convergence criterion of 0.1 kJ mol^{-1}. Only after the first energy minimization was the SHAKE algorithm used to constrain the bond lengths, allowing unfavorable interactions between side chains to be released during the initial minimization. The Cu(II) atom was stabilized in the LPMO active site using distance restraints with a force constant of 10^4 kJ mol^{-1} nm^{-2} (see Table S3 for atoms and distances), and the

DOI: 10.1021/acs.biochem.8b01178
Biochemistry 2019, 58, 1226−1235

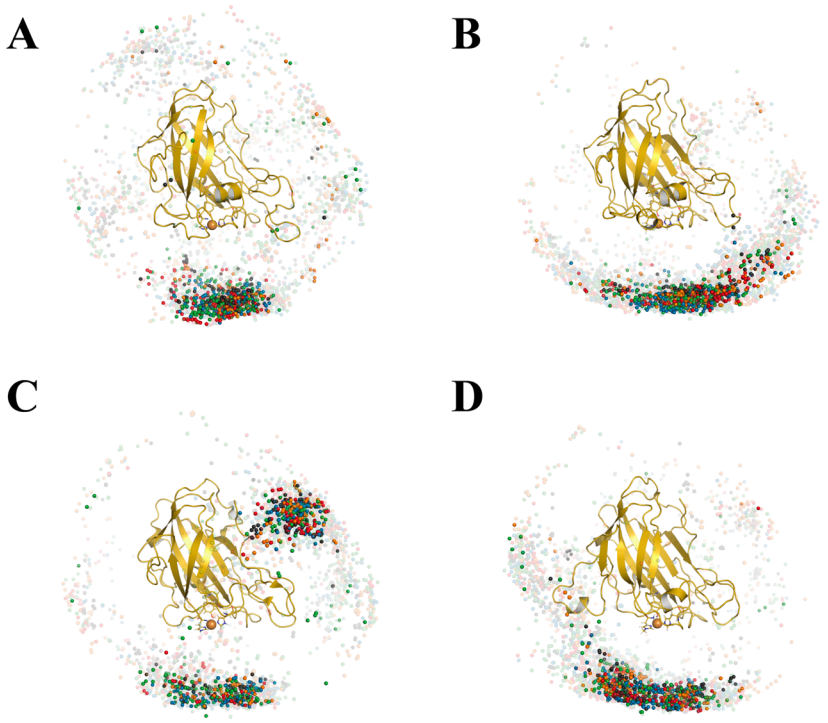

Figure 1. Distribution of CYT centers of mass (COMs) around LPMOs after *ab initio* docking. (A) *Nc*LPMO9C, (B) *Nc*LPMO9D, (C) *Nc*LPMO9F, and (D) *Nc*LPMO9M are depicted in a yellow cartoon representation, and their Cu(II) centers are shown as spheres. The CYT COMs for *Nc*CYTIIA, *Nc*CYTIIB, *Ch*CYT, *Pc*CYT, and *Ct*CYT (colored red, orange, blue, gray, and green, respectively) are shown as spheres around the LPMOs. The COMs of the last 800 out of 1000 ranked HADDOCK docking solutions are shown in reduced transparency.

iron center of CYT heme *b* was ligated to its coordinating residues (i.e., HIS176 N_ε and MET74 S) via a covalent bond to avoid any dissociation. The rotation of the individual complex units relative to each other was restrained using a dihedral angle restraint with a force constant of 0.05 kJ mol^{-1} deg^{-2}, roughly allowing a 10° deviation from the target value in either direction. This restraint was defined by four points (i–j–k–l) for every complex as shown in Table S4. The latter restraints were maintained during all of the following steps. Once the proteins were solvated in a periodic rectangular box with simple point charge (SPC) water[43] maintaining a minimum solute–wall distance of 0.8 nm, the systems were energy minimized again to remove unfavorable solute–solvent contacts. Subsequently, sodium and chloride atoms were added to ensure a neutral system charge (Table S6). Thereafter, the systems were equilibrated at 50 K with initial random velocities generated from a Maxwell–Boltzmann distribution. During five discrete steps of 20 ps, the temperature of the systems was increased to 300 K. Finally, roto-translational constraints on the CYTs were initialized in two additional equilibration steps to hamper the overall rotation of the whole complex. During the production simulations, a weak coupling scheme with coupling times τ_T = 0.1 ps and τ_P = 0.5 ps and an isothermal compressibility of 4.575 × 10^{-4} kJ^{-1} mol nm^3 were used to maintain a constant temperature of 300 K and a constant pressure of 1 atm.[44] The reaction field method[45] was used to treat nonbonded interactions with a cutoff radius of 1.4 nm and an ε of 61 to represent the medium outside the cutoff sphere. On the basis of the histograms shown in Figures S6–S11, additional simulations were added to ensure sufficient overlap for the computation of the PMF plot. At least 40 rotational states were simulated for at least 6 ns. Up to 2 ns was discarded for equilibration to ensure converged histograms. In addition, plain MD simulation of homology models and *ab initio* docking solutions were performed for 100 ns using the same settings as described above, however without the dihedral angle restraint between the two proteins. Furthermore, the force constant for the Cu(II)-coordinating distance restraints was reduced to 400 kJ mol^{-1} nm^{-2}.

Analysis. The PyMOL Molecular Graphics System (version 1.7.0.0, Schrödinger, LLC) was used to visualize and analyze the docking solutions and protein complexes resulting from the MD simulations. Geometric properties between the CYT and LPMO were calculated using the GROMOS++ software package.[36] Thereafter, the resulting dihedral angle measurements were taken as input for the weighted histogram analysis method (WHAM) script implemented in the GROMACS molecular simulation suite[46] to compute the potentials of mean force (PMFs) in a periodic manner with a bin size of 1°. Error estimates were calculated using a bootstrapping procedure with 100 repeats. A Savitzky–Golay filter was applied on the PMF data with a filter window length of 69 and a polynomial of the first order.[47,48] The following python packages were used for data analys and representation: SciPy,[48] NumPy,[49] and Matplotlib.[50]

RESULTS

Defining the Interaction Region of the CYT on LPMO.

To investigate possible interaction sites on LPMOs, guided *ab initio* docking of 20 LPMO–CYT complexes was performed. Because the interaction surface on CYTs is given by an area surrounding their heme *b* cofactors,[24] the *ab initio* docking was guided by defining accessible residues on CYTs accordingly (Table S1). As one can see in Figure 1, the centers of mass (COMs) of the 1000 best ranked individual CYT positions were scattered around the LPMOs. It is only when looking at

DOI: 10.1021/acs.biochem.8b01178
Biochemistry 2019, 58, 1226–1235

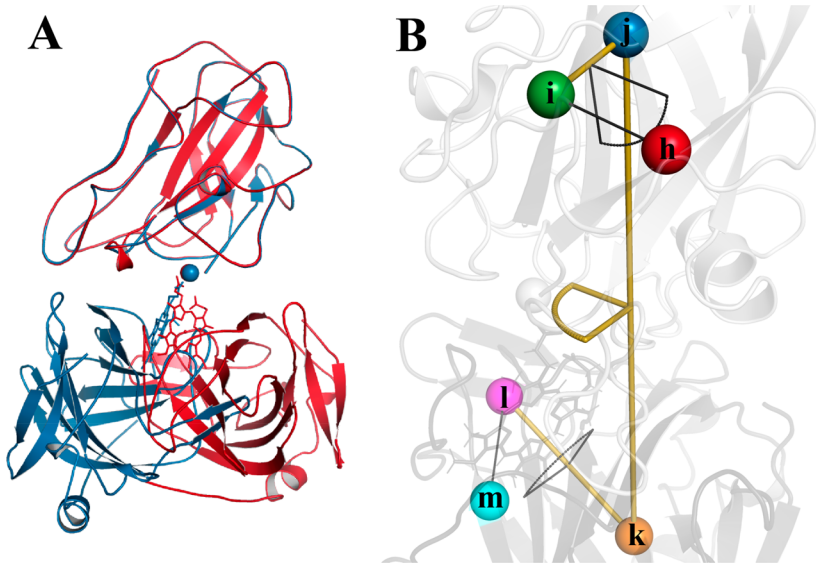

Figure 2. (A) Two clusters of restraint docking solutions of *Nc*CYTIIA with *Nc*LPMO9F. CYTs of docking poses included in cluster 1 (red) are rotated ∼160° compared to CYTs included in cluster 2 (blue) around an axis given by the LPMO COM and its copper center. (B) Representation of the atoms used for the angle (Table S4). The dihedral angle i−j−k−l (green, blue, orange, and magenta spheres, respectively) is represented by yellow lines. The h−i−j−k (red, green, blue, and orange spheres, respectively) and j−k−l−m (blue, orange, magenta, and cyan spheres, respectively) dihedral angles are shown as black lines.

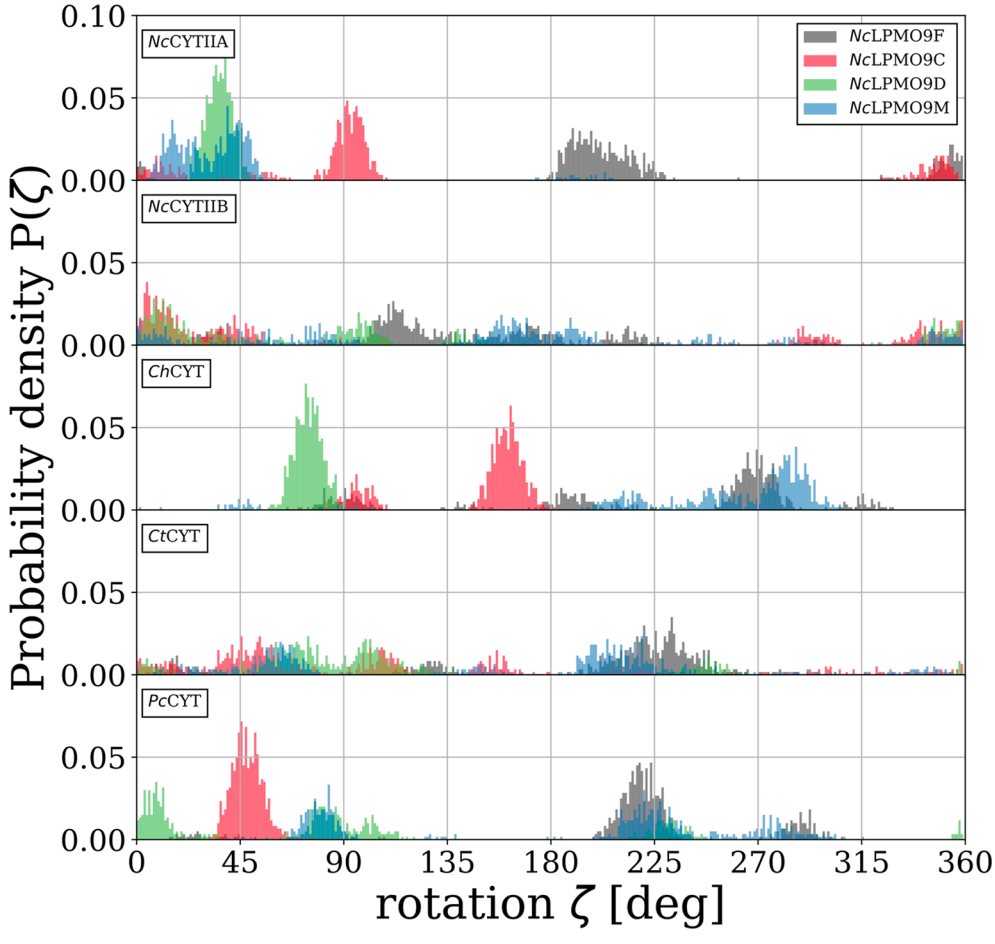

Figure 3. Dihedral angle distribution of restraint docking experiments. The i−j−k−l dihedral angle is defined as described in Table S4 (Figure 2B). Data for *Nc*LPMO9F, -9C, -9D, and -9M are colored gray, red, green, and blue, respectively. The panels separate the complexes together with *Nc*CYTIIA, *Nc*CYTIIB, *Ch*CYT, *Ct*CYT, and *Pc*CYT from top to bottom, respectively.

DOI: 10.1021/acs.biochem.8b01178
Biochemistry 2019, 58, 1226−1235

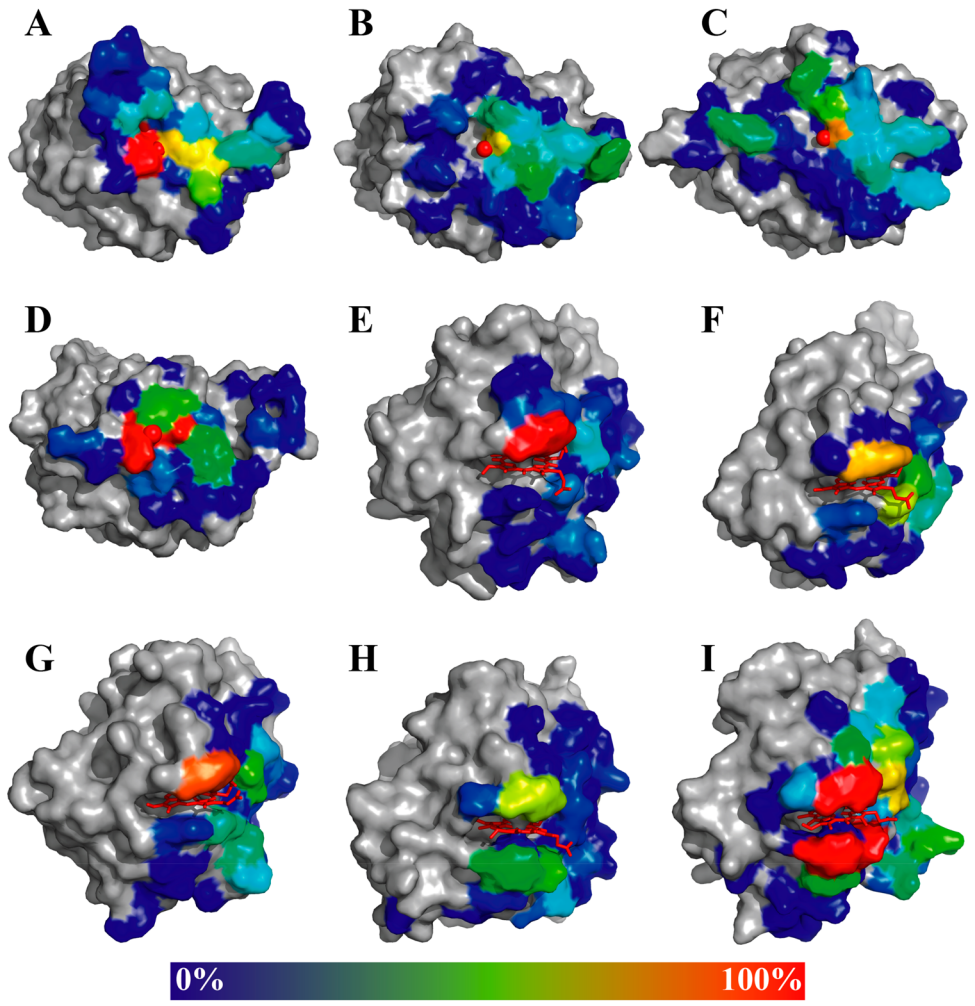

Figure 4. Heat map of the interacting residues of all of the docking poses on the CYT and LPMO surface: (A) *Nc*LPMO9F, (B) *Nc*LPMO9C, (C) *Nc*LPMO9D, (D) *Nc*LPMO9M, (E) *Ch*CYT, (F) *Pc*CYT, (G) *Nc*CYTIIA, (H) *Nc*CYTIIB, and (I) *Ct*CYT. Residues are colored according to the frequency of their involvement in interacting with any atom in the restraint docking experiments, from red (100%) to blue (>0%). Areas colored gray were not involved in the interaction.

the top fifth of the 1000 best ranked complexes that COMs separate into distinct groups (Figure 1 and Figure S2). In the case of *Nc*LPMO9C, -9D, and -9M, a majority of the COMs of *Nc*CYTIIA, *Nc*CYTIIB, *Ch*CYT, *Pc*CYT, and *Ct*CYT were in the vicinity of the LPMO Cu(II) centers (group 1), whereas only a small number of CYTs were located elsewhere around the LPMOs (panels A, B, and D, respectively of Figure 1 and Figure S2). In contrast to this clear distribution, the CYT COMs around *Nc*LPMO9F can be divided into two groups (Figure 1C). The first cluster was again in the vicinity of the LPMO Cu(II) center like group 1 described above, while the cluster of CYTs was in an area of *Nc*LPMO9F that was previously proposed as a possible binding site for the CYT.[23] The ratio between the two groups was ∼1 for all CYTs, and only a small number of CYT positions could not be assigned to either group (Figure S2). In the case of the CYT positions included in group 1, the electron tunnelling pathway as computed using the gromos++ program epath[51,52] from the heme *b* iron to the LPMO Cu(II) center measured 1.29 ± 0.03 nm and involved a single jump through space. Conversely, the electron tunnelling pathway for CYT positions included in group 2 was significantly longer (5.9 ± 0.5 nm). Furthermore, a plain MD simulation of a *Nc*LPMO9F−*Nc*CYTIIA complex from group 2 showed large fluctuations in terms of contact surface area and LPMO−heme *b* distance over time (Figure S3), which indicates a weaker interaction in this position than with the area around the copper center. As we will show below, simulations on group 1 conformations lead to significantly smaller fluctuations in these properties (Figure S4).

Refining the CYT−LPMO Complex (restraint docking). The guided *ab initio* docking was in agreement with the published data,[24,25] which suggested that the interaction region on LPMO is around its catalytic site. To predict possible modes of binding between the interaction partners allowing a direct electron transfer between CYT heme *b* and the LPMO Cu(II) center, docking experiments of the 20 CYT−LPMO combinations were performed with a distance restraint between any atom of CYT heme *b* and the LPMO Cu(II) with three different seeds. Subsequently, a clustering of the docking solutions revealed major differences in the rotation of CYT relative to LPMO, which could be measured by a dihedral angle between the two proteins (Figure 2 and Table S4). The difference in rotation between the individual complexes could reach 180° [e.g., *Nc*CYTIIA and *Nc*LPMO9F (Figure 2A)].

DOI: 10.1021/acs.biochem.8b01178
Biochemistry 2019, 58, 1226−1235

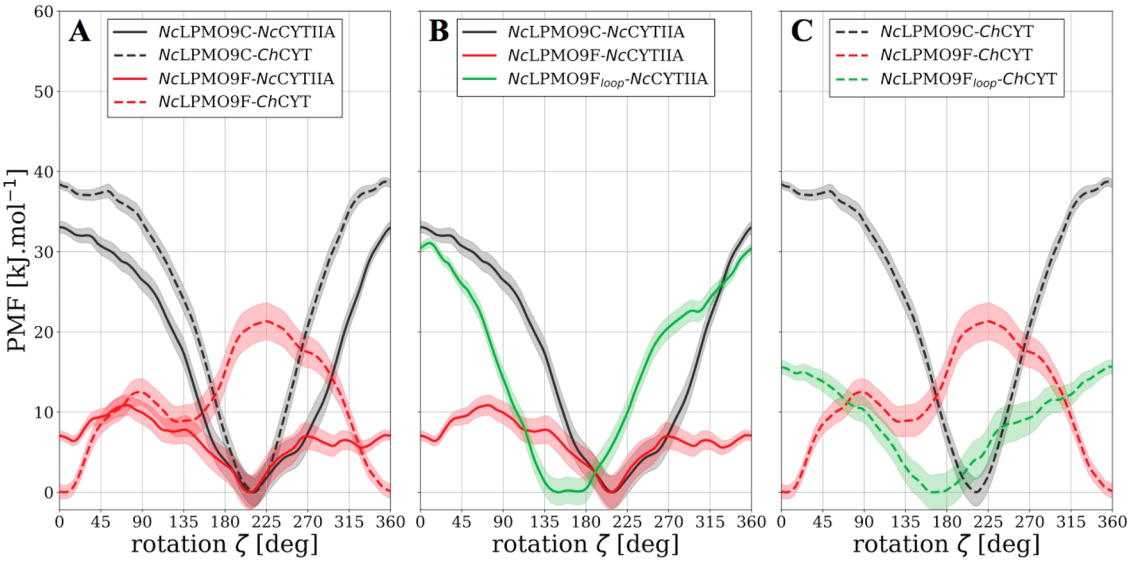

Figure 5. Potentials of mean force for various complexes. Free energy as a function of the rotation of LPMO relative to CYT. Data for *Nc*LPMO9C, -9F, and -9F$_{loop}$ are colored black, red and green, respectively. The solid and dashed lines represent data for complexes with *Nc*CYTIIA and *Ch*CYT, respectively. Shaded areas indicate bootstrap error estimates. Panel A shows the data for four wild type complexes, and panels B and C compare the results for a suggested variant to the corresponding curves of panel A.

Additionally, the resulting rotational angles hinted at the presence of distinct groups with occasional overlap (Figure 3). Furthermore, the maxima in the distribution of the rotational angle of *Nc*LPMO9C and -9D with any of the five CYTs are well-defined and consistently found between 0° and 180°. Inversely, the maxima of the rotational angle distributions of *Nc*LPMO9F and *Nc*LPMO9M complexes are located between 180° and 315° apart from those of the *Nc*CYTIIA−*Nc*LPMO9M and the *Nc*CYTIIB−*Nc*LPMO9F complexes. The presence of distribution maxima suggests the presence of multiple binding modes defined by an optimal dihedral angle between the CYT and LPMO. However, docking experiments with *Nc*CYTIIB and *Ct*CYT exhibited a more undefined distribution of rotational angles spreading from 0° to 360°, which might suggest a less specific interaction between these two CYTs and the four tested LPMOs.

A heat map of the interacting LPMO residues from all of the docking poses shows that only residues around Cu(II) significantly contribute to the interactions with the CYT (Figure 4A−D) and that the contribution is decreasing circularly from the Cu(II) center. A similar analysis of the CYT surface revealed that only the site of the surface involving the heme *b* propionate groups is involved in the docking and not the site involving the vinyl groups (Figure 4E−I). Heme *b* propionate A was observed to contact the LPMO Cu(II) in 99.7% of the docking solutions as opposed to 8.5% for heme *b* propionate D. This is readily explained by the higher accessibility of heme *b* propionate A. It is important to notice that the interaction restraint was set between any atom of CYT heme *b* and the LPMO Cu(II) center. A conserved tyrosine located next to the heme *b* propionate groups of the CYT (i.e., *Nc*CYTIIA Y99, *Nc*CYTIIB Y105, *Ch*CYT Y99, *Pc*CYT Y90, and *Ct*CYT Y97) showed a large contribution in the overall contacts, as well.

The Most Energetically Favorable Position Is Dependent on LPMO. Having a rather flat geometry, the interface between CYT and LPMO allows for multiple interaction modes in terms of the rotation relative to each other. To reveal the most favorable docking pose, multiple sets of MD simulations were performed in which the individual proteins were restrained to specific dihedral angles by a harmonic potential. From these, the free energy surface along the dihedral angles (i.e., the PMF) was computed via the weighted histogram analysis method.[46,53] To verify whether the rotational angle was influenced by the LPMO or CYT variant, at least 40 restraint MD simulations with four different LPMO−CYT complexes were performed. See the Supporting Information for the resulting dihedral angle distributions (Figures S6−S11) and a movie visualizing the rotation of *Nc*CYTIIA around *Nc*LPMO9C. Figure 5A shows the free energy landscape of *Nc*LPMO9C and *Nc*LPMO9F in complex with either *Nc*CYTIIA or *Ch*CYT. Although the calculated charges of *Nc*CYTIIA and *Ch*CYT (i.e., −3 and −15, respectively, at pH 6 with reduced heme *b*) differed notably, the energy minimum seemed to be influenced predominantly by the LPMO variant rather than the CYT. The complexes with *Nc*LPMO9C (calculated charge of 0 at pH 6 with Cu^{2+}) had a clear energy minimum at 210°, flanked by high energy barriers of 38.7 kJ mol^{-1} at 40° and 33.1 kJ mol^{-1} at 0° for *Ch*CYT and *Nc*CYTIIA, respectively. In contrast, the PMFs for complexes with *Nc*LPMO9F (calculated charge of +4 at pH 6 with Cu^{2+}) were less pronounced and shallower, with minima at 0° and 135° (*Ch*CYT) and 206° and 15° (*Nc*CYTIIA). Note that while the preference is inverted for *Ch*CYT, both CYTs can be expected to bind with angles of 0° and 160°/200°. The maximum free energies were found to be 21.3 kJ mol^{-1} at 225.5° and 11 kJ mol^{-1} at 73.5° for pairs with *Ch*CYT and *Nc*CYTIIA, respectively. Interestingly, the most unfavorable torsional angle for the *Nc*LPMO9F and *Ch*CYT complex overlaps with the minimum energy region of the other three complexes and the least favorable angle of *Nc*LPMO9C corresponds to a (local) minimum for *Nc*LPMO9F. A closer look at a snapshot from the minimum regions of complexes with *Nc*LPMO9C (Figure 6A) reveals that *Nc*LPMO9C residues H64−S82 [loop 3 (Figure 6C)] form a major component of the interaction surface with CYT. Because

DOI: 10.1021/acs.biochem.8b01178
Biochemistry 2019, 58, 1226−1235

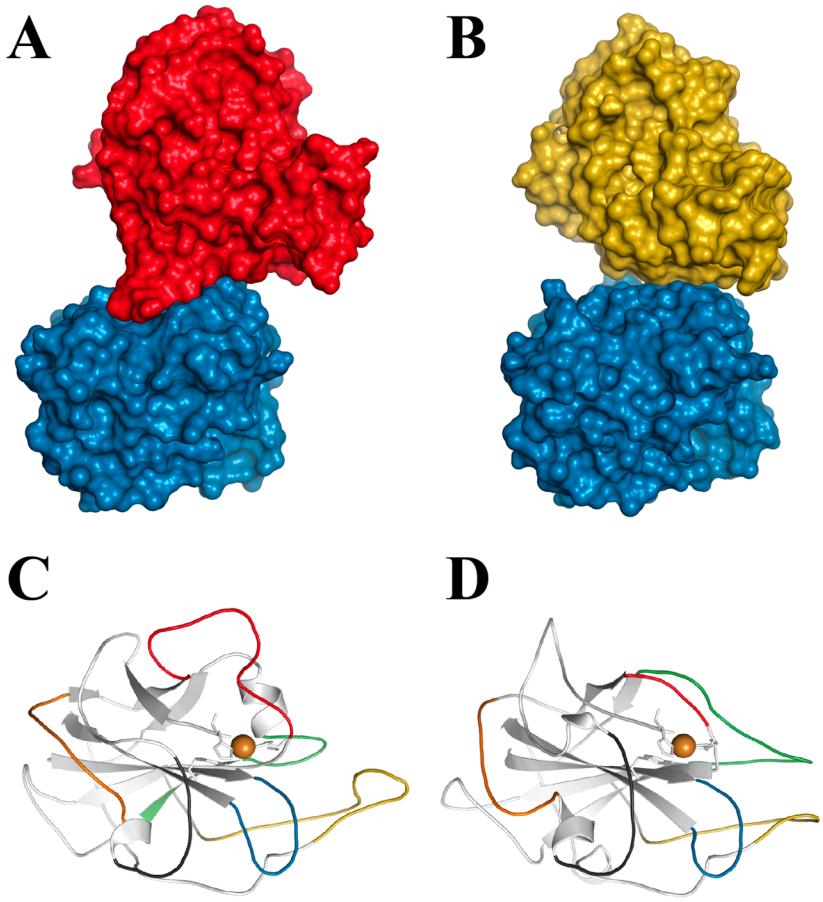

Figure 6. Selected snapshots of *Nc*CYTIIA (blue) in complex with (A) *Nc*LPMO9C (red) and (B) *Nc*LPMO9F (yellow) at dihedral angles (ζ) of 204° and 161°, respectively. *Nc*CYTIIA is in the same orientation in panels A and B. The contact surface areas are 5 and 4 nm^2 for panels A and B, respectively. Cartoon depictions of the (C) *Nc*LPMO9C and (D) *Nc*LPMO9F catalytic sites. The Cu(II) atom (brown sphere) is shown together with the histidine brace and the flanking tyrosine (stick representation). The loops around the catalytic site are numbered and colored from the N- to C-terminus as follows. Loop 1: black, *Nc*LPMO9C N27−S34 and *Nc*LPMO9F N29−S37. Loop 2: orange, *Nc*LPMO9C C39−V49 and *Nc*LPMO9F F43−T53. Loop 3: red, *Nc*LPMO9C H64−S82 and *Nc*LPMO9F P68−Y71. Loop 4: green, *Nc*LPMO9C F108−W120 and *Nc*LPMO9F Q106−S121. Loop 5: blue, *Nc*LPMO9C L154−A163 and *Nc*LPMO9F L145−A153. Loop 6: yellow, *Nc*LPMO9C N202−P222 and *Nc*LPMO9F N195−P209.

*Nc*LPMO9F loop 3 is shorter [P68−Y71 (Figure 6D)], the contribution to the interaction surface with the CYT is less pronounced and the interaction surface is reduced by 1 nm^2.

Furthermore, the entire orientation of the complex units was monitored. As one can see in Table S5 (Figure S5), the distance between the CYT and LPMO was stable around 4.5 nm within all of the simulations and the highest standard deviation that could be observed was 0.3 nm for the average of all of the *Nc*CYTIIA−*Nc*LPMO9C simulations. To ensure a proper measurement of the dihedral angle between the two proteins (i−j−k−l), the angles through atoms i, j, and k and j, k, and l were monitored (Figure 2B and Table S4). The angles were comparable during all of the simulations with averages of 64° and 72° for the i−j−k and j−k−l angles, respectively. However, on the basis of the calculated standard deviations for all of the simulations of the individual complexes, one can see that the i−j−k angle was fluctuating most with a maximum of 22° for the *Nc*CYTIIA−*Nc*LPMO9F$_{loop}$ complex. The values measured for the j−k−l angle on the other hand seemed to be more stable throughout the simulations with a maximum standard deviation of 10° (i.e., *Nc*CYTIIA−*Nc*LPMO9C and *Ch*CYT−*Nc*LPMO9F$_{loop}$). Because the proteins were also able to rotate around the axes given by atoms i and j and atoms j and k, two additional dihedral angles (h−i−j−k and j−k−l−m) were monitored. We could observe that the LPMO showed increased mobility during all of the simulations around the i−j axis and the h−i−j−k dihedral angle was around 99° on average with a maximum standard deviation of 24°. In contrast, a maximum standard deviation of 8° around the k−l axis reflected a restricted movement of the CYT.

Moreover, the surface area and the minimum distance between the two enzymes were monitored for three simulations around the minimum energy region per complex (Figure S4). It could be observed that complexes involving *Nc*LPMO9C and *Nc*LPMO9F$_{loop}$ showed a slightly larger surface area compared to those of complexes with *Nc*LPMO9F. Overall, the contact surface area is smaller than for the simulation of the group 2 complex (Figure S3). Also, the interquartile range is larger for simulations of *Nc*LPMO9C and *Nc*LPMO9F$_{loop}$ with *Nc*CYTIIA (1.4 and 1.8 nm^2, respectively) than for the remaining complexes. In all of the simulations, heme *b* propionate A was close to the LPMO, which also reflected the fact that all of the complexes were stable (Figure S4). Interestingly, in complexes with *Nc*CYTIIA, the minimum distance from heme *b* propionate D to the LPMO was comparable to that of propionate A. On the other

DOI: 10.1021/acs.biochem.8b01178
Biochemistry 2019, 58, 1226−1235

hand, in simulations with *Ch*CYT, the minimum distance between heme *b* propionate D and LPMO was generally larger than for propionate A.

Swapping a Loop around the *Nc*LPMO9F Catalytic Site Modulates the Energy Landscape. To test how the free energy profile along the rotation depends on *Nc*LPMO9C loop 3, it was introduced into the *Nc*LPMO9F model (*Nc*LPMO9F$_{loop}$). Performing the MD workflow described above with *Nc*LPMO9F$_{loop}$ had a notable influence on the shape of the PMF plot (Figure 5B,C). At 31.1 kJ mol^{-1}, the free energy barrier for the *Nc*LPMO9F$_{loop}$−*Nc*CYTIIA complex was considerably higher than that of the *Nc*LPMO9F−*Nc*CYTIIA complex. Moreover, the minimum free energy region for the *Nc*LPMO9F$_{loop}$−*Nc*CYTIIA complex was more contracted compared to that of the complex with the nonmodified *Nc*LPMO9F and the local free energy minima at 15° and 329° disappeared. Although the overall shape of the *Nc*LPMO9F$_{loop}$−*Nc*CYTIIA curve resembles the free energy profile of the *Nc*LPMO9C−*Nc*CYTIIA complex, the energy minimum is shifted by −25°. The same observations could be made for the *Nc*LPMO9F$_{loop}$−*Ch*CYT complex; however, the changes in the energy landscape were more striking compared to those in the complex with *Nc*CYTIIA. The energy minimum and maximum were shifted by 180° and 130°, respectively, for the *Nc*LPMO9F$_{loop}$−*Ch*CYT complex compared to those of the nonmodified version of the complex. The energy barrier remained at 15.7 kJ mol^{-1}. Interestingly, the energy minimum for the *Nc*LPMO9F$_{loop}$−*Ch*CYT complex overlapped with the energy minimum of the complex with *Nc*CYTIIA.

CONCLUSIONS

The *ab initio* docking experiments performed in this study confirmed that the main interaction surface on LPMO is located around the Cu(II) center. This is in agreement with recent experiments that were performed on apo-*Nc*LPMO9C without a Cu(II) and *Nc*LPMO9D in complex with *Nc*CYTIIA.[24,25] Moreover, because of the relatively flat interaction surfaces on both LPMOs and CYTs, a rotation of the two units relative to each other is possible and was observed in the restraint docking experiments. This also indicates that the CYT propionate A−LPMO copper interaction is a pivotal point in the interaction with a significant contribution to binding. An analysis of the rotation of LPMOs relative to CYTs revealed that some complexes tend to group at certain rotational angles, while very diverse docking solutions were found for *Nc*CYTIIB and *Ct*CYT. Note, however, that for these CYTs, we used homology models, possibly adding uncertainty to the predictions of the complexes. Unfortunately, the overlap between the individual LPMO−CYT rotational groups was minimal after the docking experiments. To investigate the preferred orientations more systematically and allow for larger conformational changes in the protein structures, we performed extensive umbrella sampling MD simulations. For six different LPMO−CYT complexes, we could confirm that the most favorable positions in terms of rotation of LPMO relative to CYT were between 135° and 225°. The rather broad energy minimum region agrees with a transient and relatively unspecific mode of interaction between CDH and LPMO. Previously, the low specificity of molecular recognition has been associated with electron transfer between, e.g., cytochrome *c* and its partners.[54] Moreover, we could observe that a conserved tyrosine residue (*Nc*CYTIIA Y99 and *Ch*CYT Y99) in the vicinity of CYT heme *b* can make a polar contact with the heme *b* propionate D group. Furthermore, we could show that *Nc*LPMO9C loop 3 is guiding the interaction with CYT by replacing this particular loop in *Nc*LPMO9F. The loops around the LPMO catalytic site have previously been suggested to be involved in substrate specificity[55,56] but have hitherto never been related to the interaction with CDH. *Nc*LPMO9C and -9D oxidize their substrate at the C^4 position[12,17,57] and in our calculations show well-defined preferences of the CYT−LPMO orientation. On the other hand, *Nc*LPMO9F is a C^1 oxidizer and *Nc*LPMO9M a C^1/C^4 oxidizer, which is attributed to differences in the LPMO loops.[17,55,56] Here we postulate that the differences in the loop architecture also affect the orientation of the CYT−*Nc*LPMO9F complex, which becomes less defined in our calculations when loop 3 is shorter. Overall, this work provides insight into the interaction between CYT and LPMO and emphasizes the role of the LPMO loops surrounding the LPMO catalytic site in guiding this interaction.

ASSOCIATED CONTENT

Supporting Information

The Supporting Information is available free of charge on the ACS Publications website at DOI: 10.1021/acs.biochem.8b01178.

Overview of the LPMO copper-ligating atoms, location of the 200 best ranked CYTs around the LPMOs after guided *ab initio* docking, contact surface area analysis, definition of the restraints, and analysis of the degrees of freedom and histograms for PMF calculation (PDF)

Visualization of the rotational profile of *Nc*LPMO9C and *Nc*CYTIIA (ZIP)

AUTHOR INFORMATION

Corresponding Author

*E-mail: chris.oostenbrink@boku.ac.at.

ORCID

Christophe V. F. P. Laurent: 0000-0002-9112-6981

Daniel Tunega: 0000-0003-0822-1580

Chris Oostenbrink: 0000-0002-4232-2556

Funding

The authors thank the Doctoral Programme Biomolecular Technology of Proteins (BioToP) supported by the Austrian Science Fund (FWF; W1224).

Notes

The authors declare no competing financial interest.

REFERENCES

(1) Himmel, M. E., Ding, S. Y., Johnson, D. K., Adney, W. S., Nimlos, M. R., Brady, J. W., and Foust, T. D. (2007) Biomass recalcitrance: Engineering plants and enzymes for biofuels production. *Science 315*, 804−807.

(2) Vaaje-Kolstad, G., Horn, S. J., van Aalten, D. M. F., Synstad, B., and Eijsink, V. G. H. (2005) The non-catalytic chitin-binding protein CBP21 from Serratia marcescens is essential for chitin degradation. *J. Biol. Chem. 280*, 28492−28497.

(3) Harris, P. V., Welner, D., McFarland, K. C., Re, E., Navarro Poulsen, J.-C., Brown, K., Salbo, R., Ding, H., Vlasenko, E., Merino, S., Xu, F., Cherry, J., Larsen, S., and Lo Leggio, L. (2010) Stimulation of lignocellulosic biomass hydrolysis by proteins of glycoside hydrolase family 61: Structure and function of a large, enigmatic family. *Biochemistry 49*, 3305−3316.

DOI: 10.1021/acs.biochem.8b01178
Biochemistry 2019, 58, 1226−1235

(4) Eijsink, V. G. H., Vaaje-Kolstad, G., Vårum, K. M., and Horn, S. J. (2008) Towards new enzymes for biofuels: lessons from Chitinase research. *Trends Biotechnol. 26*, 228−235.
(5) Vaaje-Kolstad, G., Westereng, B., Horn, S. J., Liu, Z., Zhai, H., Sørlie, M., and Eijsink, V. G. H. (2010) An oxidative enzyme boosting the enzymatic conversion of recalcitrant polysaccharides. *Science 330*, 219−222.
(6) Levasseur, A., Drula, E., Lombard, V., Coutinho, P. M., and Henrissat, B. (2013) Expansion of the enzymatic repertoire of the CAZy database to integrate auxiliary redox enzymes. *Biotechnol. Biofuels 6*, 41.
(7) Hemsworth, G. R., Henrissat, B., Davies, G. J., and Walton, P. H. (2014) Discovery and characterization of a new family of lytic polysaccharide monooxygenases. *Nat. Chem. Biol. 10*, 122−126.
(8) Vu, V. V., Beeson, W. T., Span, E. A., Farquhar, E. R., and Marletta, M. A. (2014) A family of starch-active polysaccharide monooxygenases. *Proc. Natl. Acad. Sci. U. S. A. 111*, 13822−13827.
(9) Couturier, M., Ladevèze, S., Sulzenbacher, G., Ciano, L., Fanuel, M., Moreau, C., Villares, A., Cathala, B., Chaspoul, F., Frandsen, K. E., Labourel, A., Herpoël-Gimbert, I., Grisel, S., Haon, M., Lenfant, N., Rogniaux, H., Ropartz, D., Davies, G. J., Rosso, M.-N., Walton, P. H., Henrissat, B., and Berrin, J.-G. (2018) Lytic xylan oxidases from wood-decay fungi unlock biomass degradation. *Nat. Chem. Biol. 14*, 306−310.
(10) Sabbadin, F., Hemsworth, G. R., Ciano, L., Henrissat, B., Dupree, P., Tryfona, T., Marques, R. D. S., Sweeney, S. T., Besser, K., Elias, L., Pesante, G., Li, Y., Dowle, A. A., Bates, R., Gomez, L. D., Simister, R., Davies, G. J., Walton, P. H., Bruce, N. C., and McQueen-Mason, S. J. (2018) An ancient family of lytic polysaccharide monooxygenases with roles in arthropod development and biomass digestion. *Nat. Commun. 9*, 756.
(11) Tan, T.-C., Kracher, D., Gandini, R., Sygmund, C., Kittl, R., Haltrich, D., Hallberg, B. M., Ludwig, R., and Divne, C. (2015) Structural basis for cellobiose dehydrogenase action during oxidative cellulose degradation. *Nat. Commun. 6*, 7542.
(12) Beeson, W. T., Phillips, C. M., Cate, J. H. D., and Marletta, M. A. (2012) Oxidative cleavage of cellulose by fungal copper-dependent polysaccharide monooxygenases. *J. Am. Chem. Soc. 134*, 890−892.
(13) Bissaro, B., Røhr, Å. K., Müller, G., Chylenski, P., Skaugen, M., Forsberg, Z., Horn, S. J., Vaaje-Kolstad, G., and Eijsink, V. G. H. (2017) Oxidative cleavage of polysaccharides by monocopper enzymes depends on H2O2. *Nat. Chem. Biol. 13*, 1123−1128.
(14) Hangasky, J. A., Iavarone, A. T., and Marletta, M. A. (2018) Reactivity of O2 versus H2O2 with polysaccharide monooxygenases. *Proc. Natl. Acad. Sci. U. S. A. 115*, 4915−4920.
(15) Quinlan, R. J., Sweeney, M. D., Lo Leggio, L., Otten, H., Poulsen, J.-C. N., Johansen, K. S., Krogh, K. B. R. M., Jørgensen, C. I., Tovborg, M., Anthonsen, A., Tryfona, T., Walter, C. P., Dupree, P., Xu, F., Davies, G. J., and Walton, P. H. (2011) Insights into the oxidative degradation of cellulose by a copper metalloenzyme that exploits biomass components. *Proc. Natl. Acad. Sci. U. S. A. 108*, 15079−15084.
(16) Cannella, D., Möllers, K. B., Frigaard, N.-U., Jensen, P. E., Bjerrum, M. J., Johansen, K. S., and Felby, C. (2016) Light-driven oxidation of polysaccharides by photosynthetic pigments and a metalloenzyme. *Nat. Commun. 7*, 11134.
(17) Kracher, D., Scheiblbrandner, S., Felice, A. K. G., Breslmayr, E., Preims, M., Ludwicka, K., Haltrich, D., Eijsink, V. G. H., and Ludwig, R. (2016) Extracellular electron transfer systems fuel cellulose oxidative degradation. *Science 352*, 1098−1101.
(18) Hyde, S. M., and Wood, P. M. (1997) A Mechanism for Production of Hydroxyl Radicals by the Brown-Rot Fungus Coniophora Puteana: Fe(III) Reduction by Cellobiose Dehydrogenase and Fe(II) Oxidation at a Distance from the Hyphae. *Microbiology 143*, 259−266.
(19) Zamocky, M., Ludwig, R., Peterbauer, C. K., Hallberg, B. M., Divne, C., Nicholls, P., and Haltrich, D. (2006) Cellobiose Dehydrogenase − A Flavocytochrome from Wood-Degrading, Phytopathogenic and Saprotropic Fungi. *Curr. Protein Pept. Sci. 7*, 255−280.
(20) Kracher, D., Zahma, K., Schulz, C., Sygmund, C., Gorton, L., and Ludwig, R. (2015) Inter-domain electron transfer in cellobiose dehydrogenase: modulation by pH and divalent cations. *FEBS J. 282*, 3136−3148.
(21) Harada, H., Onoda, A., Uchihashi, T., Watanabe, H., Sunagawa, N., Samejima, M., Igarashi, K., and Hayashi, T. (2017) Interdomain flip-flop motion visualized in flavocytochrome cellobiose dehydrogenase using high-speed atomic force microscopy during catalysis. *Chem. Sci. 8*, 6561−6565.
(22) Kadek, A., Kavan, D., Marcoux, J., Stojko, J., Felice, A. K. G., Cianférani, S., Ludwig, R., Halada, P., and Man, P. (2017) Interdomain electron transfer in cellobiose dehydrogenase is governed by surface electrostatics. *Biochim. Biophys. Acta, Gen. Subj. 1861*, 157−167.
(23) Li, X., Beeson, W. T., IV, Phillips, C. M., Marletta, M. A., and Cate, J. H. D. (2012) Structural basis for substrate targeting and catalysis by fungal polysaccharide monooxygenases. *Structure 20*, 1051−1061.
(24) Courtade, G., Wimmer, R., Røhr, Å. K., Preims, M., Felice, A. K. G., Dimarogona, M., Vaaje-Kolstad, G., Sørlie, M., Sandgren, M., Ludwig, R., Eijsink, V. G. H., and Aachmann, F. L. (2016) Interactions of a fungal lytic polysaccharide monooxygenase with β-glucan substrates and cellobiose dehydrogenase. *Proc. Natl. Acad. Sci. U. S. A. 113*, 5922−5927.
(25) Bodenheimer, A. M., O'Dell, W. B., Oliver, R. C., Qian, S., Stanley, C. B., and Meilleur, F. (2018) Structural investigation of cellobiose dehydrogenase IIA: Insights from small angle scattering into intra- and intermolecular electron transfer mechanisms. *Biochim. Biophys. Acta, Gen. Subj. 1862*, 1031−1039.
(26) Arnold, K., Bordoli, L., Kopp, J., and Schwede, T. (2006) The SWISS-MODEL workspace: a web-based environment for protein structure homology modelling. *Bioinformatics 22*, 195−201.
(27) Benkert, P., Biasini, M., and Schwede, T. (2011) Toward the estimation of the absolute quality of individual protein structure models. *Bioinformatics 27*, 343−350.
(28) Biasini, M., Bienert, S., Waterhouse, A., Arnold, K., Studer, G., Schmidt, T., Kiefer, F., Cassarino, T. G., Bertoni, M., Bordoli, L., and Schwede, T. (2014) SWISS-MODEL: Modelling protein tertiary and quaternary structure using evolutionary information. *Nucleic Acids Res. 42*, W252−W258.
(29) Schmid, N., Christ, C. D., Christen, M., Eichenberger, A. P., and van Gunsteren, W. F. (2012) Architecture, implementation and parallelisation of the GROMOS software for biomolecular simulation. *Comput. Phys. Commun. 183*, 890−903.
(30) Schmid, N., Eichenberger, A. P., Choutko, A., Riniker, S., Winger, M., Mark, A. E., and van Gunsteren, W. F. (2011) Definition and testing of the GROMOS force-field versions 54A7 and 54B7. *Eur. Biophys. J. 40*, 843−856.
(31) Li, H., Robertson, A. D., and Jensen, J. H. (2005) Very fast empirical prediction and rationalization of protein pKa values. *Proteins: Struct., Funct., Genet. 61*, 704−721.
(32) Bas, D. C., Rogers, D. M., and Jensen, J. H. (2008) Very fast prediction and rationalization of pKa values for protein−ligand complexes. *Proteins: Struct., Funct., Genet. 73*, 765−783.
(33) Olsson, M. H. M., Søndergaard, C. R., Rostkowski, M., and Jensen, J. H. (2011) PROPKA3: Consistent Treatment of Internal and Surface Residues in Empirical pKa Predictions. *J. Chem. Theory Comput. 7*, 525−537.
(34) Dominguez, C., Boelens, R., and Bonvin, A. M. J. J. (2003) HADDOCK: A Protein−Protein Docking Approach Based on Biochemical or Biophysical Information. *J. Am. Chem. Soc. 125*, 1731−1737.
(35) de Vries, S. J., van Dijk, A. D. J., Krzeminski, M., van Dijk, M., Thureau, A., Hsu, V., Wassenaar, T., and Bonvin, A. M. J. J. (2007) HADDOCK versus HADDOCK: New features and performance of HADDOCK2.0 on the CAPRI targets. *Proteins: Struct., Funct., Genet. 69*, 726−733.

DOI: 10.1021/acs.biochem.8b01178
Biochemistry 2019, 58, 1226−1235

(36) Eichenberger, A. P., Allison, J. R., Dolenc, J., Geerke, D. P., Horta, B. A. C., Meier, K., Oostenbrink, C., Schmid, N., Steiner, D., Wang, D., and van Gunsteren, W. F. (2011) GROMOS++ Software for the Analysis of Biomolecular Simulation Trajectories. *J. Chem. Theory Comput. 7*, 3379−3390.
(37) Torrie, G. M., and Valleau, J. P. (1977) Nonphysical sampling distributions in Monte Carlo free-energy estimation: Umbrella sampling. *J. Comput. Phys. 23*, 187−199.
(38) Zou, C., Larisika, M., Nagy, G., Srajer, J., Oostenbrink, C., Chen, X., Knoll, W., Liedberg, B., and Nowak, C. (2013) Two-Dimensional Heterospectral Correlation Analysis of the Redox-Induced Conformational Transition in Cytochrome c Using Surface-Enhanced Raman and Infrared Absorption Spectroscopies on a Two-Layer Gold Surface. *J. Phys. Chem. B 117*, 9606−9614.
(39) Frisch, M. J., Trucks, G. W., Schlegel, H. B., Scuseria, G. E., Robb, M. A., Cheeseman, J. R., Scalmani, G., Barone, V., Petersson, G. A., Nakatsuji, H., Li, X., Caricato, M., Marenich, A., Bloino, J., Janesko, B. G., Gomperts, R., Mennucci, B., Hratchian, H. P., Ortiz, J. V., Izmaylov, A. F., Sonnenberg, J. L., Williams-Young, D., Ding, F., Lipparini, F., Egidi, F., Goings, J., Peng, B., Petrone, A., Henderson, T., Ranasinghe, D., Zakrzewski, V. G., Gao, J., Rega, N., Zheng, G., Liang, W., Hada, M., Ehara, M., Toyota, K., Fukuda, R., Hasegawa, J., Ishida, M., Nakajima, T., Honda, Y., Kitao, O., Nakai, H., Vreven, T., Throssell, K., Montgomery, J. A., Jr., Peralta, J. E., Ogliaro, F., Bearpark, M., Heyd, J. J., Brothers, E., Kudin, K. N., Staroverov, V. N., Keith, T., Kobayashi, R., Normand, J., Raghavachari, K., Rendell, A., Burant, J. C., Iyengar, S. S., Tomasi, J., Cossi, M., Millam, J. M., Klene, M., Adamo, C., Cammi, R., Ochterski, J. W., Martin, R. L., Morokuma, K., Farkas, O., Foresman, J. B., and Fox, D. J. (2009) *Gaussian 09*, revision A.02, Gaussian Inc., Wallingford, CT.
(40) Perdew, J. P., Burke, K., and Ernzerhof, M. (1996) Generalized Gradient Approximation Made Simple. *Phys. Rev. Lett. 77*, 3865−3868.
(41) Weigend, F., and Ahlrichs, R. (2005) Balanced basis sets of split valence, triple zeta valence and quadruple zeta valence quality for H to Rn: Design and assessment of accuracy. *Phys. Chem. Chem. Phys. 7*, 3297−3305.
(42) Reed, A. E., Weinstock, R. B., and Weinhold, F. (1985) Natural population analysis. *J. Chem. Phys. 83*, 735−746.
(43) Berendsen, H. J. C., Postma, J. P. M., van Gunsteren, W. F., and Hermans, J. (1981) Interaction Models for Water in Relation to Protein Hydration. In *Intermolecular Forces. The Jerusalem Symposia on Quantum Chemistry and Biochemistry* (Pullman, B., Ed.) Vol. *14*, pp 331−342, Springer, Dordrecht, The Netherlands.
(44) Berendsen, H. J. C., Postma, J. P. M., van Gunsteren, W. F., Dinola, A., and Haak, J. R. (1984) Molecular dynamics with coupling to an external bath. *J. Chem. Phys. 81*, 3684−3690.
(45) Tironi, I. G., Sperb, R., Smith, P. E., and van Gunsteren, W. F. (1995) A generalized reaction field method for molecular dynamics simulations. *J. Chem. Phys. 102*, 5451−5459.
(46) Hub, J. S., de Groot, B. L., and van der Spoel, D. (2010) g_whams - A Free Weighted Histogram Analysis Implementation Including Robust Error and Autocorrelation Estimates. *J. Chem. Theory Comput. 6*, 3713−3720.
(47) Savitzky, A., and Golay, M. J. E. (1964) Smoothing and Differentiation of Data by Simplified Least Squares Procedures. *Anal. Chem. 36*, 1627−1639.
(48) Jones, E., Oliphant, T., Peterson, P., et al. (2001) {SciPy}: Open source scientific tools for {Python}.
(49) Oliphant, T. E. *A Guide to NumPy*, 1st ed., Trelgol Publishing.
(50) Hunter, J. D. (2007) Matplotlib: A 2D Graphics Environment. *Comput. Sci. Eng. 9*, 90−95.
(51) Sündermann, A., and Oostenbrink, C. (2013) Molecular dynamics simulations give insight into the conformational change, complex formation, and electron transfer pathway for cytochrome P450 reductase. *Protein Sci. 22*, 1183−1195.
(52) Beratan, D. N., Onuchic, J. N., Betts, J. N., Bowler, B. E., and Gray, H. B. (1990) Electron-Tunneling Pathways in Ruthenated Proteins. *J. Am. Chem. Soc. 112*, 7915−7921.
(53) Kumar, S., Rosenberg, J. M., Bouzida, D., Swendsen, R. H., and Kollman, P. A. (1992) The weighted histogram analysis method for free-energy calculations on biomolecules. I. The method. *J. Comput. Chem. 13*, 1011−1021.
(54) McLendon, G., and Hake, R. (1992) Interprotein electron transfer. *Chem. Rev. 92*, 481−490.
(55) Vu, V. V., Beeson, W. T., Phillips, C. M., Cate, J. H. D., and Marletta, M. A. (2014) Determinants of Regioselective Hydroxylation in the Fungal Polysaccharide Monooxygenases. *J. Am. Chem. Soc. 136*, 562−565.
(56) Danneels, B., Tanghe, M., and Desmet, T. (2018) Structural Features on the Substrate-Binding Surface of Fungal Lytic Polysaccharide Monooxygenases Determine Their Oxidative Regioselectivity. *Biotechnol. J.*, DOI: 10.1002/biot.201800211.
(57) Isaksen, T., Westereng, B., Aachmann, F. L., Agger, J. W., Kracher, D., Kittl, R., Ludwig, R., Haltrich, D., Eijsink, V. G. H., and Horn, S. J. (2014) A C4-oxidizing lytic polysaccharide monooxygenase cleaving both cellulose and cello-oligosaccharides. *J. Biol. Chem. 289*, 2632−2642.

DOI: 10.1021/acs.biochem.8b01178
Biochemistry 2019, 58, 1226−1235